# 3' Nucleotide Asymmetry Directs miRNA Strand Selection

Jeffrey C. Medley[1], Sumire Kurosu Moriya[1], Huiwu Ouyang[2], Heather Crawshaw[1], Sarah Y. Zhang[1], Ganesh Panzade[1,3], Will J. Sydzyik[1], Joel T. Sydzyik[1,4], Mira Bhandari[1,5], Christopher M. Hammell[2] and Anna Zinovyeva[1]*

[1] Division of Biology, Kansas State University. Manhattan, KS.
[2] Cold Spring Harbor Laboratory. Cold Spring Harbor, NY.
[3]Laboratory of Human Retrovirology and Immunoinformatics, Frederick National Laboratory for Cancer Research, Frederick, MD.
[4] University of Kansas School of Medicine, Kansas City, KS.
[5] Department of Molecular Genetics and Cell Biology, University of Chicago. Chicago, IL.
*Corresponding author. Email: zinovyeva@ksu.edu

## Abstract

Accurate microRNA (miRNA) strand selection is essential for defining the regulatory landscape of the miRNA-induced silencing complex (miRISC). While 5′ nucleotide identity and duplex thermodynamics have been proposed to bias strand choice, these features cannot fully explain in vivo strand preferences. Here, we uncover a conserved and previously unrecognized role for 3′ nucleotide asymmetry in directing miRNA strand selection in *Caenorhabditis elegans* and human cells. A favorable 3′ terminal nucleotide on the passenger strand promotes selective loading of the opposing guide strand into miRISC, revealing a cooperative interplay between 5′ and 3′ terminal asymmetries that ensures precise strand discrimination. These findings establish a unified, evolutionarily conserved mechanism for miRNA duplex sorting and expand the fundamental rules governing small RNA biogenesis.

## Introduction

The biogenesis of miRNAs is integral to their biological activity, as the precise sequence of mature miRNAs must be preserved to maintain sequence-specific interactions with mRNA targets (*1*, *2*). Primary miRNA (pri-miRNA) transcripts are processed in the nucleus by the Microprocessor complex to produce stem-loop miRNA precursors (pre-miRNA) (*3–6*). Following nuclear export, Dicer cleaves pre-miRNAs to generate partially double-stranded ~22 nucleotide duplexes containing characteristic two-nucleotide 3' overhangs (*7–12*). The miRNA duplex is subsequently loaded into an Argonaute protein, which selectively anchors a single, mature strand to initiate formation of the miRNA induced silencing complex (miRISC) (*13*, *14*). Although the strands originating from either the 5' (5p) or 3' (3p) arms of the pre-miRNA are competent for Argonaute loading (*15–17*), asymmetric strand selection usually leads to a dominant guide strand and a less abundant passenger strand that is rapidly degraded after release from Argonaute (*18*). For some miRNAs, strand selection occurs in a more symmetrical fashion where both strands appear to function as mature miRNAs (*19*, *20*). Differences in miRNA strand usage have also been observed in different cellular, tissular and developmental contexts, suggesting that strand selection is a regulated process (*19*, *21–24*). As miRNA-dependent gene regulation is sequence dependent, alternative miRNA strand choice is expected to lead to broad changes in target selection. Consistently, aberrant miRNA strand selection has also been reported in several human diseases including cancers, although the mechanisms leading to alternative strand selection in human disease are not fully understood (*18*).

Argonaute plays a direct role in strand selection and favors loading the duplex end containing a favorable 5' nucleotide (U>A>C>G) and lower thermodynamic stability in vitro (*16*, *17*, *25*, *26*). The 5' nucleotide of the guide strand is embedded within a pocket in the MID domain of Argonaute, which has a strong preference for uracil (*13*, *14*, *25*). Several residues within the Argonaute MID and PIWI domains directly contact the phosphate backbone of the guide strand (*13*, *14*) and may serve as a sensor for thermodynamic asymmetry (*17*). The twin-drive model postulates that miRNA strand selection can be predicted by modeling the relative effects of 5' nucleotide identity and thermodynamic asymmetry (*17*). However, this model fails to explain strand selection of ~25% of miRNAs that have unfavorable 5' nucleotides and more stable 5' ends (*18*), suggesting that additional asymmetries influence miRNA strand selection in vivo.

Here, we used genome editing to alter endogenous *C. elegans* miRNAs and evaluated the relative contributions of 5' nucleotide identity and thermodynamic asymmetry in vivo. Consistent with previous findings, we show that a 5' uracil is favorable for stand choice, and that unpaired 5' nucleotides are strongly selected regardless of nucleotide identity. However, we found that duplexes with symmetrical 5' nucleotides and thermodynamic end stabilities underwent asymmetric strand selection, suggesting that additional features outside of the 5' end contribute to strand choice. We identified a strong bias for cytosine at the 3' end of passenger strands in *C. elegans*. Mutating the 3' nucleotide of symmetrical duplexes was sufficient to reverse strand selection, suggesting that 3' nucleotide identity influences miRNA strand asymmetry in vivo. In duplexes with asymmetric 5' ends, 3' nucleotide asymmetry had a lesser effect on strand choice, indicating that various nucleotide asymmetries coordinately drive miRNA strand selection. By expressing exogenous miRNA variants in human HEK293T cells, we show that 3' nucleotide asymmetry plays a conserved role in miRNA strand selection, although a 3' cytosine on

passenger strands was less preferred in human cells. Collectively, our results support a model where nucleotide asymmetries on both strands of miRNA duplexes promote asymmetric strand selection.

## Results

### Characterization of *C. elegans* miRNA duplexes

To better understand how 5' nucleotide identity and thermodynamic asymmetries are linked to miRNA strand selection, we profiled the duplex characteristics of *C. elegans* miRNAs (Table S1). The preferred guide strand is expected to have a favorable 5' nucleotide and lower 5' end stability than the corresponding passenger strand (Fig. 1A). Consistent with previous observations (*27*), the majority of *C. elegans* guide strands have a 5' uracil, whereas passenger strands lack an obvious 5' nucleotide bias (Fig. 1B). To examine thermodynamic asymmetry, we used free energy values of *C. elegans* miRNA duplex ends from a previous study (*28*). As expected, the average stability of duplex ends corresponding to guide strands was lower than passenger strands (Fig. 1C, Table S1). We observed thermodynamic asymmetry when considering the first through fourth terminal nucleotides, with the largest asymmetry observed for three terminal nucleotides (Fig. 1C). Thus, strand selection of *C. elegans* miRNAs is correlated to 5' nucleotide identity and thermodynamic asymmetry.

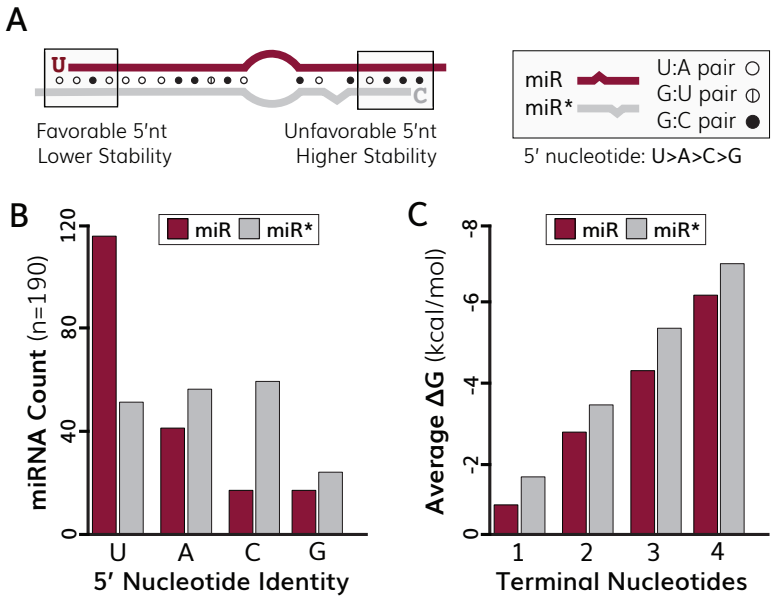


**Fig 1. Duplex characteristics of *C. elegans* miRNAs.** (A) Duplex features associated with miRNA strand selection. The guide (miR) end of typically contains a favorable 5' nucleotide and lower thermodynamic stability than the passenger (miR*) duplex end. The guide strand is shown in maroon, and the passenger strand is shown in gray. U:A pairs are illustrated by an open circle, G:U wobble pairs are indicated by an open circle with a vertical line and G:C pairs are represented by closed circles. The sizes of bulges and mismatched nucleotides are drawn to scale. (B) Quantification of 5' nucleotide identity for *C. elegans* miRNA guide (maroon) and passenger strands (gray). n is given as the number of miRNA duplexes quantified (C) Quantification of the free energy of miRNA duplex ends corresponding to guide (maroon) and passenger (gray) duplex ends. Free energy values were calculated by in silico unwinding (*28*) of the terminal 1:4 nucleotides of each duplex end.

95 **A favorable 5' nucleotide is not sufficient to drive miRNA strand selection in vivo**
96
97 To address whether 5' nucleotide identity and thermodynamic asymmetry directly influence
98 miRNA strand choice in vivo, we used genome editing to alter the duplex properties of
99 endogenous *C. elegans* miRNAs. We first examined a series of mutations in the *mir-58a*, *mir-1*
100 and *mir-2* miRNAs that primarily impacted the identity of 5' nucleotides (Fig. 2, Table S2). Both
101 strands of the miR-58 duplex have a favorable 5' uracil, whereas only the guide strands of miR-1
102 and miR-2 have a 5' uracil (Fig. 2). We used RNAcofold to determine how each miRNA
103 variation affected the thermodynamic stability of the terminal three nucleotides for each duplex
104 end (*28*) (Table S3). For all three miRNAs, the guide duplex end has a lower stability than the
105 passenger duplex end (Fig. 2). Based on predictions from the twin-drive model (*17*), the four
106 miR-58 mutations (M1-M4) should switch strand selection, the miR-1-M1 mutation should
107 retain normal strand choice, and the miR-2-M1 mutation should choose both duplex strands
108 indiscriminately leading to equal accumulation of both strands (Table S4).
109
110 To investigate how miRNA mutations affect strand selection, we performed small RNA
111 sequencing in L4-staged animals (Tables S5 and S6), a developmental stage where miR-58, miR-
112 1 and miR-2 have relatively high expression (*29*). The miR-58-M1 and miR-58-M2 mutations
113 change the 5' uracil of the guide strand to less favorable nucleotides (adenine and guanine
114 respectively), which results in the 5' nucleotide of the guide strand becoming unpaired, thereby
115 modestly reducing duplex end stability (Fig. 2A). In the miR-58-M3 mutation, we introduced a
116 compensatory mutation in the passenger strand that restores base pairing to the 5' adenine variant
117 (Fig. 2A). Our analysis revealed that miR-58-M1 and miR-58-M2 retain normal strand choice,
118 while miR-58-M3 accumulated both duplex strands at near equal levels (Fig. 2A). As the
119 primary difference between the miR-58-M1 and miR-58-M3 mutations is the base-pairing status
120 of the 5' nucleotide, these results suggest that unpaired 5' nucleotides are highly favorable for
121 strand selection and can override a preferrable 5' nucleotide on the other strand. Consistently, the
122 miR-58-M4 mutation, which alters the 3' end of the guide strand to disrupt base-pairing of the 5'
123 nucleotide on the passenger strand, appeared to select the passenger strand although total miR-58
124 levels were reduced (Fig. 2A).
125
126 Both miR-1-M1 and miR-2-M1 mutations change a terminal C:G pair on the passenger end of
127 the duplex into a U:G wobble pair, such that both duplex strands have a symmetrical 5' uracil
128 and similar thermodynamic end stabilities (Figs. 2B and 2C). For the miR-1-M1 mutation, we
129 observed some accumulation of passenger strand, however, the miR-1-M1 mutation also
130 appeared to affect mature miR-1 levels (Fig. 2B). On the other hand, we found that the miR-2-
131 M1 mutation caused a reversal of miR-2 strand selection (Fig. 2C). Given that the miR-2-M1
132 mutation has symmetrical 5' nucleotide identity and thermodynamic end stability (Fig. 2C), this
133 suggests that additional factors likely drive asymmetric strand selection of miR-2. Notably, our
134 data show that the twin-drive model poorly predicted the actual strand preference of these
135 miRNA mutants (Table S4). We conclude that 5' nucleotide identity directly influences miRNA
136 strand selection in vivo, although favorable 5' nucleotides are not sufficient to drive asymmetric
137 strand choice, particularly when the 5' nucleotide of one strand is unpaired.
138

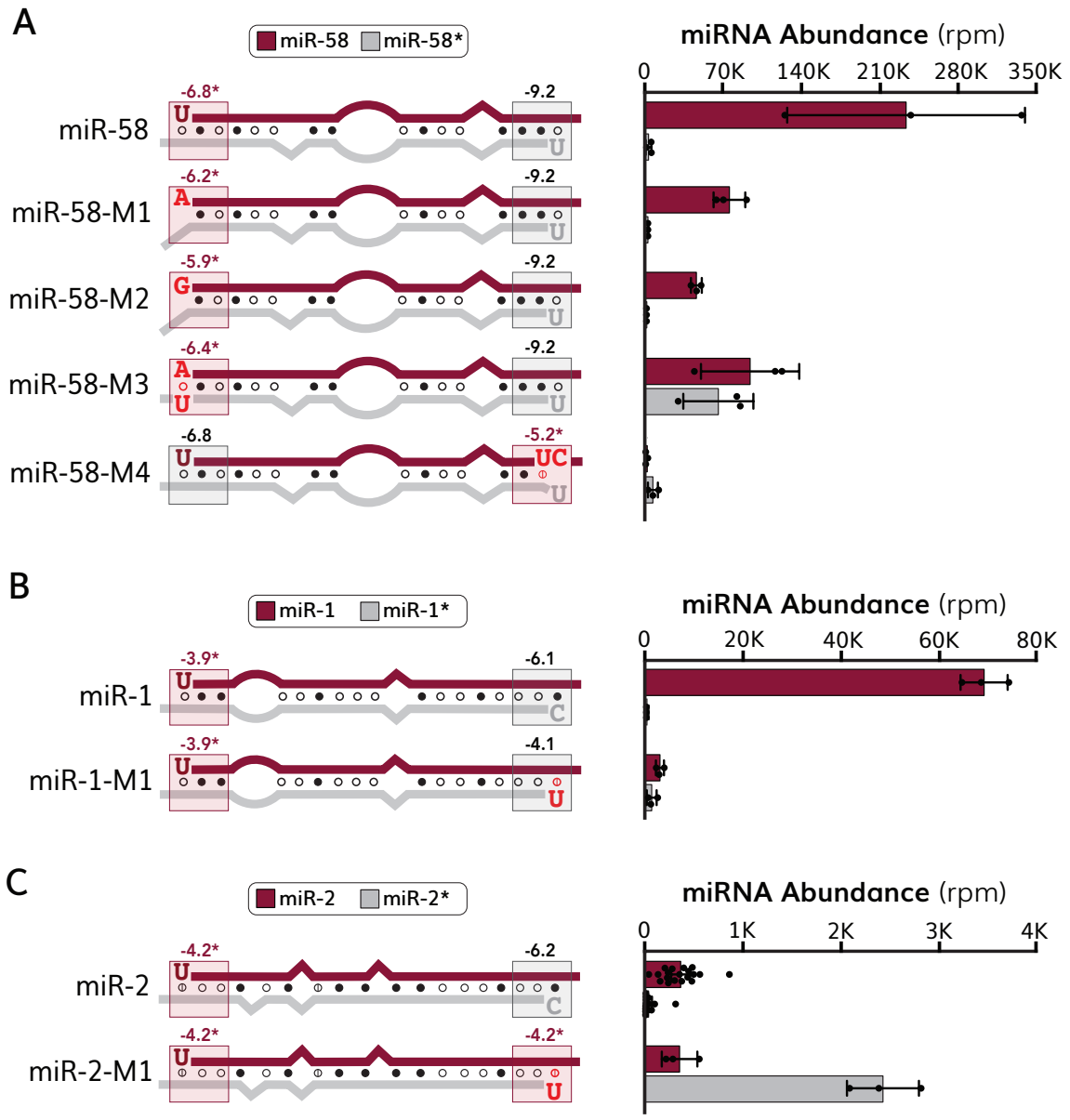


**Fig 2. 5' nucleotide identity influences miRNA strand selection in vivo.** (Left) Schematic representations of (A) miR-58, (B) miR-1 and (C) miR-2 duplex mutations that affect 5' nucleotide identity. (A-C) The guide strand is shown in maroon, and the passenger strand is shown in gray. Mutated nucleotides are indicated by red text. U:A pairs are illustrated by an open circle, G:U wobble pairs are indicated by an open circle with a vertical line and G:C pairs are represented by closed circles. Free energy values (kcal/mol) of the terminal three nucleotides (boxed) are shown on each duplex end. The less stable duplex end is marked with an asterisk and highlighted in a light red box. RNAcofold was used to predict duplex structures at 20°C. (Right) Quantification of small RNA sequencing results for (A) miR-58, (B) miR-1 and (C) miR-2. Data are presented as mean ± standard deviation, with each dot representing quantification from a single library using the NEXTFLEX v3 Small RNA Sequencing Kit. Maroon bars correspond to miRNA guide strands and gray bars represent miRNA passenger strands. Normalization was performed by dividing raw read counts by total mapped miRNA reads and multiplying by one million to acquire reads per million (rpm) values.

140 **Thermodynamic asymmetry is largely dispensable for miRNA strand choice**
141
142 We next examined mutations affecting thermodynamic asymmetry of *mir-58a*, *mir-1* and *mir-2*
143 (Fig. 3). The miR-58-M5, miR-58-M6 and miR-58-M7 mutations reduce thermodynamic end
144 stability without altering 5' nucleotide identity (Fig. 3A). The twin-drive model (*17*) predicted
145 each of these mutations, except for miR-58-M6 and miR-1-M2, to switch strands (Table S4).
146 Small RNA sequencing of L4-staged animals (Tables S5 and S6) showed that the symmetrical
147 miR-58-M5 and miR-58-M6 mutants asymmetrically selected the canonical miR-58 guide strand
148 (Fig. 3A). Furthermore, while miR-58-M7 mutants accumulated some passenger strands, they
149 did not switch strand preference, despite the passenger duplex end having lower stability (Fig.
150 3A). This observation suggested factors outside 5' nucleotide identity and thermodynamic
151 asymmetry promote strand selection of miR-58.
152
153 The more egregious miR-58-M8, miR-58-M9 and miR-58-M10 mutations reduce the stability of
154 the passenger duplex end while also introducing an unfavorable 5' nucleotide to the guide strand
155 (Fig. 3A). The miR-58-M8 and miR-58-M10 mutations both reversed strand selection,
156 demonstrating that there is not a barrier to selecting the miR-58 passenger strand (Fig. 3A).
157 While the miR-58-M9 mutation did not appear to switch strands, we observed a substantial
158 reduction in mature miR-58 levels (Fig. 3A), which was associated with a significant increase in
159 *pri-mir-58* levels, suggesting ineffective processing of *pri-mir-58* (Fig. S1A). We did not
160 observe significant changes in the levels or strand selection of the *mir-58* family members *mir-*
161 *80*, *mir-81* or *mir-82* (*30*), supporting our observations are specific to *mir-58* (Fig. S2).
162
163 The miR-1-M2, miR-1-M3 and miR-1-M4 mutations affect thermodynamic asymmetry while
164 also introducing a 5' uracil to the passenger strand; the 5' nucleotide of the miR-1 guide strand is
165 also mutated to a less favorable cytosine in miR-1-M4 mutants (Fig. 3B). We found that the
166 miR-1-M2 and miR-1-M3 mutations both preferred selection of the canonical miR-1 guide
167 strand, while miR-1-M4 asymmetrically selected the passenger strand (Fig. 3B). We observed a
168 reduction in mature miR-1 levels in each of the miR-1 mutants that we generated in this study
169 (Figs. 2B and 3B), possibly due to decreased *mir-1* expression as *pri-mir-1* levels were
170 significantly reduced in miR-1-M4 mutants (Fig. S1B). The miR-2-M2 and miR-2-M3 mutations
171 incorporate a favorable 5' uracil to the miR-2 passenger strand, while also introducing cytosines
172 to the 5' end of the miR-2 guide strand that increase the stability of the guide duplex end (Fig.
173 3C). The miR-2-M2 and miR-2-M3 mutations both resulted in highly asymmetric selection of
174 the miR-2 passenger strand and appeared to increase mature miR-2 levels (Fig. 3C). We
175 observed modest effects on *pri-mir-2* levels in miR-2 mutants, suggesting that any effects on
176 mature miR-2 levels likely occur downstream of miRNA biogenesis (Fig. S1C). Notably, the
177 twin-drive model poorly predicted the strand preference of most miRNA mutants (Table S4,
178 Figure S3), suggesting additional factors contribute to strand selection in vivo. Absolute
179 quantification of select miRNA mutants agreed with our small RNA sequencing analysis (Fig.
180 S4). Further, we observed phenotypes consistent with loss of guide strand activity in strand
181 switching mutants (Fig. S5). In the *mir-58* family mutant background, the miR-58-M8, miR-58-
182 M9 and miR-58-M10 mutations caused a reduction in adult body size, consistent with loss of
183 *mir-58* function (*30*) (Fig. S5A-B). Similarly, our *mir-1* and *mir-2* mutants showed resistance to
184 levamisole and aldicarb respectively, as previously reported for loss of *mir-1* (*31*) and *mir-2* (*32*)
185 function (Fig. S5C-D).
186

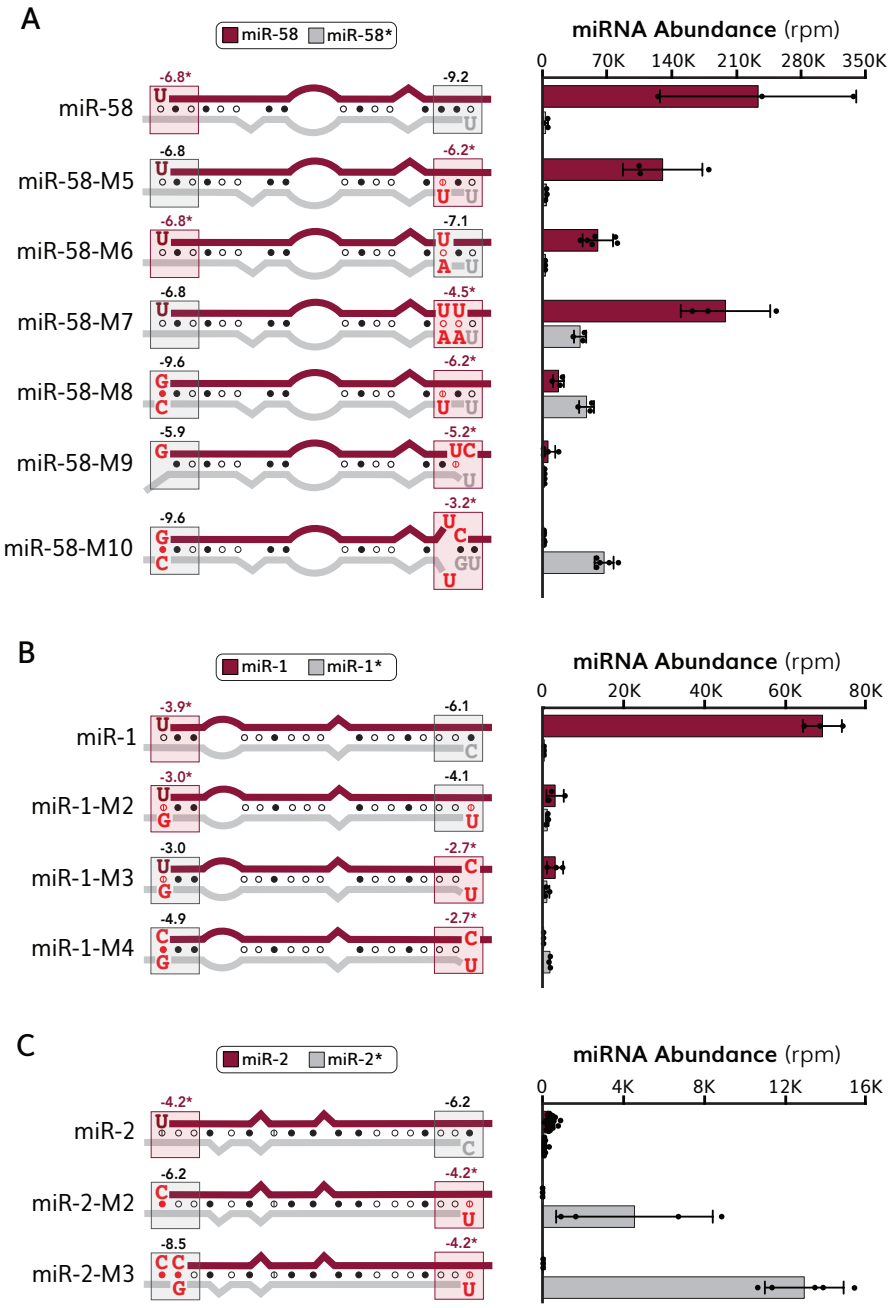


**Fig 3. Thermodynamic asymmetry is dispensable for miRNA strand selection**. (Left) Schematic representations of (A) miR-58, (B) miR-1 and (C) miR-2 duplex mutations that affect the relative thermodynamic stability of each duplex end. (A-C) The guide strand is shown in maroon, and the passenger strand is shown in gray. Mutated nucleotides are indicated by red text. U:A pairs are illustrated by an open circle, G:U wobble pairs are indicated by an open circle with a vertical line and G:C pairs are represented by closed circles. Free energy values (kcal/mol) of the terminal three nucleotides (boxed) are shown on each duplex end. The less stable duplex end is marked with an asterisk and highlighted in a light red box. RNAcofold was used to predict duplex structures at 20°C. (Right) Quantification of small RNA sequencing results for (A) miR-58, (B) miR-1 and (C) miR-2. Data are presented as mean ± standard deviation, with each dot representing quantification from a single library using the NEXTFLEX v3 Small RNA Sequencing Kit. Maroon bars correspond to miRNA guide strands and gray bars represent miRNA passenger strands. Normalization was performed by dividing raw read counts by total mapped miRNA reads and multiplying by one million to acquire reads per million (rpm) values.

187 To address whether miRNA biogenesis was affected in miRNA mutants, we quantified how each
188 mutation affected isomiR populations. With a few exceptions, most of the miR-58 variants did
189 not significantly affect the distribution of isomiRs for guide or passenger strands compared to
190 controls, suggesting that miRNA mutations do not affect production of the expected mature
191 miRNA (Fig. S6, Tables S7 and S8). In miR-58-M4, miR-58-M9 and miR-58-M10 mutants, a
192 four-base truncation of the 3' end of the guide strand was more abundant than the canonical
193 guide sequence without affecting isomiRs for passenger strands (Fig. S6, Tables S7 and S8).
194 Each of these three mutations contain the same CA:UC mutation towards the 3' end of the guide
195 strand (Table S2), which may impact processing of these mutants, as we observed for miR-58-
196 M9 (Fig. S1A), or could adversely affect the stability of the 3' end of the miRNA within the
197 Argonaute PAZ domain (*13*, *14*, *33*, *34*) thereby leading to trimming of exposed 3' ends (*35*, *36*).
198 Similarly, the miR-1-M4 mutation accumulated a one-base truncation of the 3' end of the
199 canonical guide strand without affecting passenger strand isomiRs, while isomiR populations
200 appeared unaffected for other miR-1 mutants (Fig. S8A-B, Table S9). The isomiR populations of
201 miR-2 appeared to be more dynamic, including two abundant 3' truncations of passenger strands
202 in wildtype animals (Fig. S7C-D, Tables S10 and S11). Interestingly, passenger strand isomiRs
203 were reduced in miR-2 mutants compared to wildtype, suggesting increased precision of
204 generating the expected mature sequence (Fig. S7C-D). The miR-2-M2 and miR-2-M3 mutants,
205 which asymmetrically select the miR-2 passenger strand (Fig. 3F), also altered the isomiR
206 frequency of the miR-2 guide strand (Fig. S7C-D). Thus, while most of the miRNA mutants do
207 not significantly affect isomiR populations, changes in isomiR populations were more frequently
208 observed for passenger strands of highly asymmetric miRNAs. It is possible that certain isomiRs
209 have altered duplex properties that promote their own strand selection, thereby leading to their
210 increased representation relative to the corresponding canonical miRNA, without impacting the
211 actual rate of isomiR formation. For example, in miR-2-M2 mutants, the most abundant guide
212 strand isomiR was a truncation of the 5' cytosine resulting in a more favorable 5' adenine (Fig.
213 S7C-D). Collectively, our data support a model where the identity and base-pairing status of 5'
214 nucleotides promotes miRNA strand selection but is not sufficient to explain strand preference in
215 vivo.
216
217 **Identification of duplex asymmetries associated with miRNA strand choice**
218
219 As we observed asymmetric strand selection for duplexes with symmetrical 5' ends (Figs. 2 and
220 3), we hypothesized that additional duplex features influence miRNA asymmetry in vivo. As we
221 were unable to identify additional asymmetries within the first four nucleotides on the 5' end of
222 guide and passenger strands (Fig. 4A), we next turned our attention to the 3' end of duplexes and
223 identified two nucleotide biases (Fig. 4B). The first bias was an adenine in the third-to-final
224 position of miRNA passenger strands, which was noticeably enriched among the 30 highest
225 expressed miRNAs in L4-staged animals (Fig. 4B) that represent more than 90% of total miRNA
226 reads and have more confident passenger strand annotations (*37*) (Fig. 4C). As miRNA duplexes
227 typically contain single stranded 2-nucleotide 3' overhangs (*38*, *39*), this adenine bias likely
228 reflects base paring to the preferred 5' uracil of guide strands. The second bias was the presence
229 of a 3' terminal cytosine on miRNA passenger strands, which was less frequently observed on
230 guide strands and nearly absent from the 3' ends of highly expressed miRNAs (Fig. 4B). As the
231 levels of many miRNAs are developmentally regulated, we next examined whether this 3'
232 cytosine bias was present throughout animal development or specific to the L4-stage. Using an

existing small RNA sequencing dataset (*29*), we quantified the observed 3' nucleotide identity of miRNA guide and passenger strands throughout *C. elegans* development (Fig. 4D). Throughout animal development, we found that very few guide strands ended with a 3' cytosine, whereas cytosine was among the most frequent 3' nucleotides of passenger strands (Fig. 4D). Thus, 3' nucleotide asymmetry is associated with miRNA strand choice throughout *C. elegans* development.

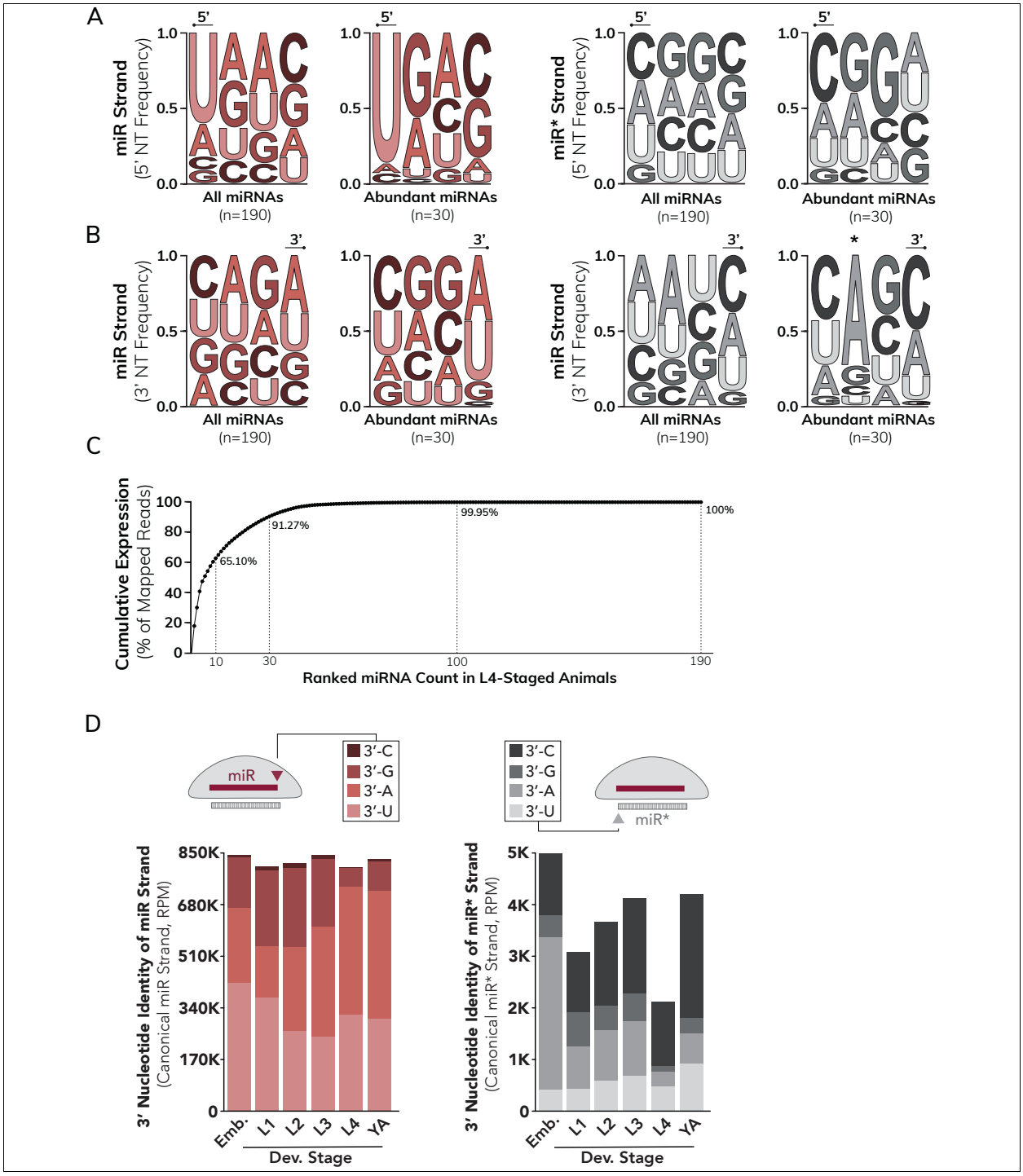

**Fig 4.** *C. elegans* miRNA duplex asymmetries. (A) Sequence logo representation of 5' nucleotide frequencies for *C. elegans* miRNA guide (left) and passenger (right) strands. (B) Sequence logo representation of 3' nucleotide frequencies for *C. elegans* miRNA guide (left) and passenger (right) strands. Asterisk indicates the third nucleotide from the 3' duplex end of the passenger strand that is adjacent to the 3' dinucleotide overhang and is expected to base pair to the 5' nucleotide of the guide strand. (A-B) Sequences are given in 5'-3' orientation, with the 5' or 3' terminal nucleotides indicated by a bulbed line above. Sequence logos were created using the weblogo3 server and colors were modified using Adobe illustrator. (C) Cumulative expression of *C. elegans* miRNAs at L4-stage. Each dot represents one miRNA (guide and passenger strands), plotted in order of most abundant to least abundant. The 10 most abundant miRNAs account for ~65% and the 30 most abundant miRNAs represent >90% of all miRNA sequencing reads at the L4 stage. (D) Quantification of 3' nucleotide frequency for miRNA guide (left) and passenger (right) strands throughout *C. elegans* development. Stacked bar graphs represent the normalized abundance of canonical miRNA guide or passenger strands (not including isomiRs) sorted by terminal 3' nucleotide identity. Schematic (top) illustrates an example of a miRNA duplex loaded into Argonaute (gray) and the arrowhead indicates the position of the 3' nucleotide of the guide (left) or passenger (right) strand. Developmental small RNA sequencing data were acquired from a previous study (*29*).

240

241 **A 3' cytosine on miRNA passenger strands promotes strand selection in *C. elegans***

242

243 To examine whether 3' nucleotide identity influences miRNA strand selection in vivo, we
244 created an additional set of *mir-58* mutations that alter 3' nucleotide identity in the wildtype or
245 symmetrical miR-58-M6 duplexes (Fig. 5, Table S2). The passenger strand of miR-58 has a 3'
246 cytosine and the guide strand has a 3' uracil (Fig. 5A). We generated mutants where the 3'
247 nucleotide of both strands were swapped, or the 3' nucleotide of one strand was mutated to
248 produce duplexes containing symmetrical 3' nucleotides (Fig. 5A). While swapping the 3'
249 nucleotide of the wild type miR-58 duplex in miR-58-M14 mutants was not sufficient to reverse
250 strand selection, swapping the 3' nucleotides of the miR-58-M6 duplex in miR-58-M16 mutants
251 reversed strand preference (Figure 5A, Tables S5 and S6). This observation suggests a novel role
252 for 3' nucleotide identity in directing miRNA strand choice. Interestingly, in the miR-58-M6
253 background, we observed near equal levels of both guide and passenger strands for the miR-58-
254 M17 mutant where both strands have 3' cytosine, but asymmetric selection of the miR-58 guide
255 strand in miR-58-M18 mutants where both strands have 3' uracil (Fig. 5A). Thus, a specific
256 preference for 3' cytosine on passenger strands appears to regulate strand selection of miR-58.

257

258 We next examined 3' nucleotide mutations of *mir-2*, which has a 3' guanine on the passenger
259 strand and a 3' cytosine on the guide strand (Fig. 5B). To minimize the effect of 5' nucleotide
260 identity, we mutated the miR-2-M1 duplex where both miR-2 strands have a symmetrical 5'
261 uracil (Fig. 5B, Table S1). The miR-2-M4 mutation switches the 3' nucleotides of each miR-2-
262 M1 strand and the miR-2-M5 mutations mutates the 3' nucleotide of the miR-2-M1 passenger
263 strand so that both strands have a symmetrical 3' guanine (Fig. 5B). The miR-2-M1 mutation
264 reversed strand preference of miR-2 (Figs. 2B and 5B) presumably due to the 3' cytosine on the
265 canonical miR-2 guide strand (passenger strand of miR-2-M1) (Fig. 5B). This passenger strand
266 accumulation in miR-2-M1 was relieved by mutation of the 3' cytosine on the miR-2 guide
267 strand in miR-2-M4 and miR-2-M5 mutants, consistent with a 3' cytosine directing strand
268 selection of miR-2 (Fig. 5B). Analysis of miR-2 (Fig. S7C-D, Tables S10 and S11) and miR-58
269 isomiRs (Fig. S6, Tables S7 and S8) indicated that the 3' nucleotide variants were processed
270 correctly. Furthermore, introducing a 3' cytosine to the guide strand of miR-71 (Fig. 5C, Table
271 S2) promoted selection of the miR-71 passenger strand without affecting isomiR populations
272 (Fig. S8, Table S12). Introducing a 3' cytosine to either strand of the miR-48 duplex (Table S2)
273 led to a small accumulation of the opposing strand without affecting miR-48 processing (Fig. S8,

Table S13). Collectively, these data show that 3' nucleotide identity influences the strand selection of a wide range of miRNAs in vivo.

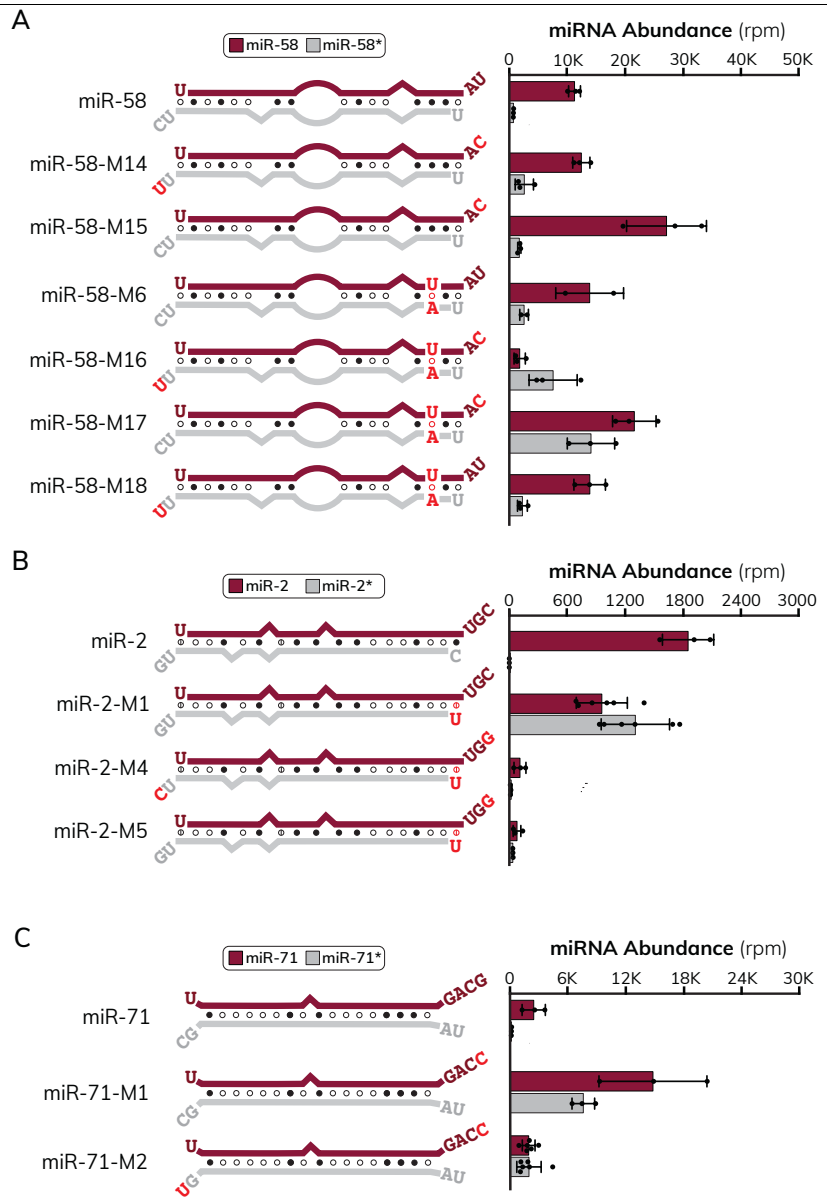


**Fig 5. A 3' cytosine on miRNA passenger strands is favorable for guide strand choice in *C. elegans*.** (Left) Schematic representations of (A) miR-58, (B) miR-2 and (C) miR-71 duplex mutations that affect 3' nucleotide identity. (A-C) The guide strand is shown in maroon, and the passenger strand is shown in gray. The nucleotide composition of dinucleotide overhang are shown for each strand. Note that the guide strand of miR-2 has an atypical trinucleotide overhang at its 3' end. Mutated nucleotides are indicated by red text. U:A pairs are illustrated by an open circle, G:U wobble pairs are indicated by an open circle with a vertical line and G:C pairs are represented by closed circles. RNAcofold was used to predict duplex structures at 20°C. (Right) Quantification of small RNA sequencing results for (A) miR-58 (B) miR-2, and (C) miR-71. Data are presented as mean ± standard deviation, with each dot representing quantification from a single library using the NEXTFLEX v4 Small RNA Sequencing Kit. Maroon bars correspond to miRNA guide strands and gray bars represent miRNA passenger strands. Normalization was performed by dividing raw read counts by total mapped miRNA reads and multiplying by one million to acquire reads per million (rpm) values.

277 The nucleotide composition of 3' overhangs may influence strand asymmetry, as we observed
278 modest differences in strand selection when we swapped 3' nucleotides or the dinucleotide
279 overhangs of miR-58 duplexes (Fig. S9). However, we did not identify obvious nucleotide
280 asymmetries beyond the terminal nucleotide of 3' ends, so we chose to focus on the role of 3'
281 nucleotide identity in this study (Fig. 4B). We next asked whether 3' nucleotide identity might be
282 directly recognized by Argonaute. To address this, we mutated a putative 3' nucleotide binding
283 pocket (*17*) that is positioned near the 5' nucleotide binding pocket in the MID domain (*13*, *14*,
284 *25*) of the *C. elegans* miRNA-associated Argonaute ALG-1 (Fig. S10A-B). Although small RNA
285 sequencing did not identify miRNA strand switching in ALG-$1^{7A}$ mutants, we observed
286 accumulation of several miRNA passenger strands (Fig. S10C, Table S6), suggesting that the
287 interaction between 3' nucleotides and Argonaute may, at least in part, promote accurate strand
288 selection. Collectively, our results suggest that a 3' cytosine on miRNA passenger strands
289 promotes guide strand selection and is sufficient to direct strand selection of miRNAs with
290 symmetrical 5' duplex ends.
291
292 **3' nucleotide identity plays a conserved role in directing miRNA choice**
293
294 We next asked whether 3' nucleotide identity influences miRNA strand selection in an
295 evolutionarily conserved fashion. We used the shERWOOD UltramiR system (*40*) to introduce a
296 set of miR-58 variants into human HEK293T cells (Fig. 6A). The human genome does not
297 encode a miR-58 homolog, which allowed us to track the strand preference of the exogenous
298 miR-58 variants. We first transfected the wildtype miR-58 and symmetrical miR-58-M6
299 duplexes as well as their respective 3' nucleotide swapped variants miR-58-M14 and miR-58-
300 M16 (Fig. 6A). Our small RNA sequencing (Table S14) showed that the canonical miR-58 guide
301 strand is asymmetrically selected, like what is observed in *C. elegans* (Fig. 6A). However, unlike
302 in *C. elegans*, both strands of the symmetrical miR-58-M6 duplex appear to be selected at near
303 equal frequency (Fig. 6A), suggesting an inherent difference in miRNA strand selection between
304 *C. elegans* and humans. Furthermore, we found that passenger strand levels were reduced in the
305 3' nucleotide swapped variants miR-58-M14 and miR-58-M16 that each have a 3' cytosine on the
306 miRNA guide strand (Fig. 6A), suggesting 3' cytosine is less favored in human cells. Each of the
307 miR-58 variants appeared to be processed correctly based on isomiR analysis (Fig. S11, Table
308 S15). However, an additional set of mutations that we designed in a modified version of the
309 human miR-339 duplex were not processed as expected (Fig. S11, Table S15), despite a modest
310 effect on strand asymmetry by those mutations (Table S14).
311
312 To characterize the 3' nucleotide preference in human cells, we created several miR-58-M6
313 duplexes comprising 16 possible 3' nucleotide combinations for each duplex strand (Fig. 6B). To
314 quantify the levels of each miR-58 variant, we performed absolute quantification for each duplex
315 strand (Fig. 6C, Table S16). We found that a 3' guanine on the guide (3p) strand of miR-58-M6
316 and a 3' uracil on the passenger (5p) strand of miR-58-M6 were most favorable for guide strand
317 selection (Fig. 6B). Notably, when each miR-58-M6 strand contained a 3' uracil or adenine, the
318 3p strand was highly favored whereas when each strand contained a 3' guanine or cytosine the 5p
319 strand was asymmetrically selected (Fig. 6B). These observations suggest that precursor origin
320 may influence miRNA strand choice, or that additional duplex features, such as 3' overhang
321 composition, may play a prominent role in directing miRNA strand choice in human cells. We
322 were unable to identify an obvious nucleotide bias at the 3' end of human miRNA duplexes (Fig.

6C-D, Table S17), consistent with the idea that additional duplex features may influence strand asymmetry in human cells. Collectively, our results indicate that 3' nucleotide asymmetry plays an evolutionarily conserved role in regulating miRNA strand choice. While it is unclear how 3' nucleotide asymmetry is recognized, we propose two alternative hypotheses that are not mutually exclusive, where the 3' nucleotide is directly bound by Argonaute or by an accessory protein to facilitate guide strand selection and passenger strand removal (Fig. 6E).

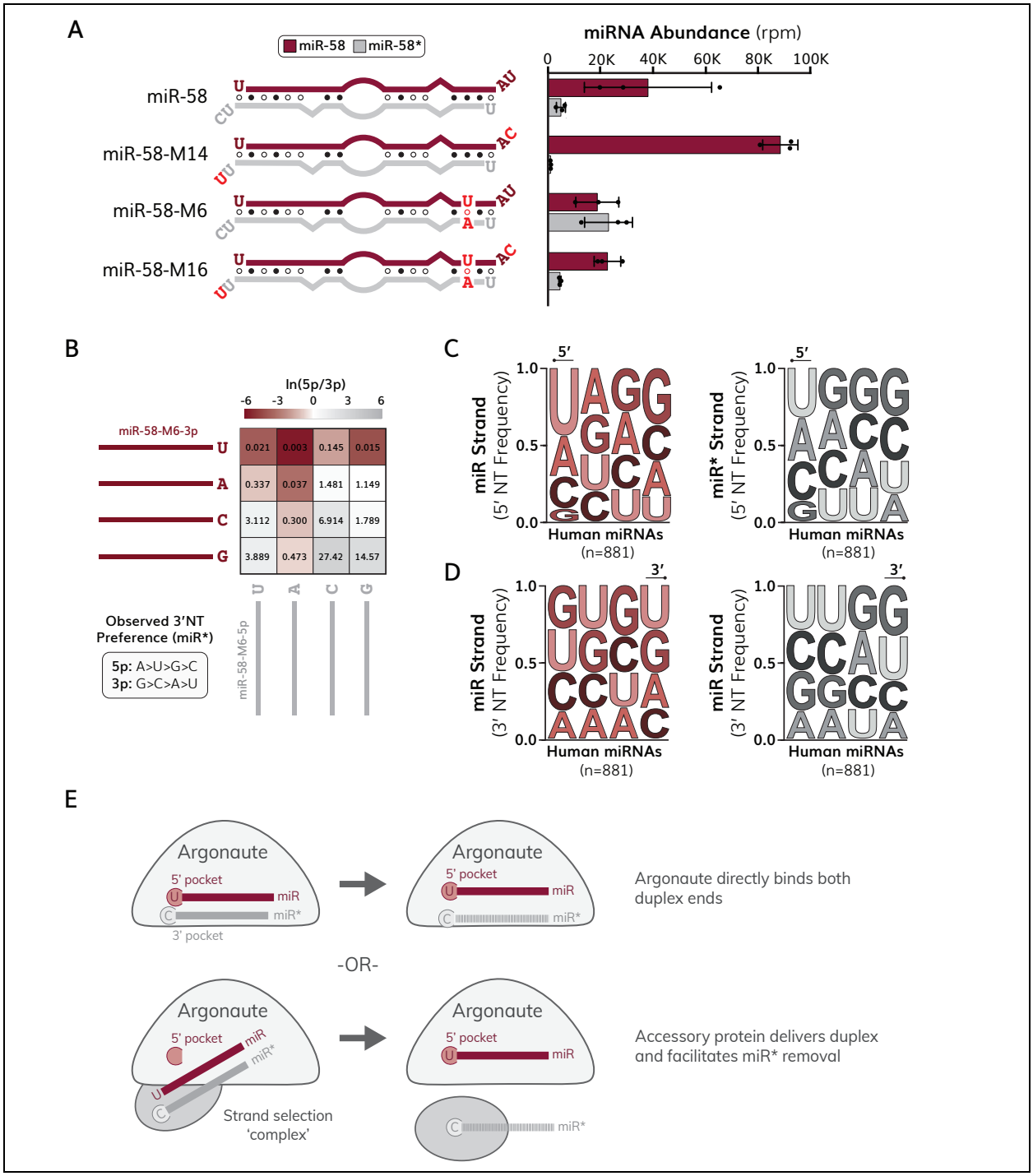

**Figure 6. 3' nucleotide identity influences miRNA strand asymmetry in human HEK293T cells.** (A) (Left) Schematic representations of exogenous miR-58 duplexes transfected into HEK293T cells that alter 3' nucleotide identity. The canonical miR-58 guide strand (from *C. elegans*) is shown in maroon, and the passenger strand is shown in gray. The nucleotide composition of dinucleotide overhang are shown for each strand. U:A pairs are illustrated by an open circle, G:U wobble pairs are indicated by an open circle with a vertical line and G:C pairs are represented by closed circles. RNAcofold was used to predict duplex structures at 37°C. (Right) Quantification of small RNA sequencing results for transfected miR-58 variants. Data are presented as mean ± standard deviation, with each dot representing quantification from a single library using the NEXTFLEX v4 Small RNA Sequencing Kit. Maroon bars correspond to canonical miRNA guide strands and gray bars represent canonical miRNA passenger strands. Normalization was performed by dividing raw read counts by total mapped miRNA reads and multiplying by one million to acquire reads per million (rpm) values. (B) Absolute quantification of miR-58-M6 duplex variants comprising each combination of 3' nucleotides on each duplex strand. Heatmap illustrates calculated ln(5p/3p) strand ratios where a deeper maroon color indicates preference for the miR-58-M6-3p (guide) strand. The non-transformed 5p/3p strand ratios are given in each box. (C) Sequence logo representation of 5' nucleotide frequencies for human miRNA guide (left) and passenger (right) strands. (D) Sequence logo representation of 3' nucleotide frequencies for human miRNA guide (left) and passenger (right) strands. (C-D) Sequences are given in 5'-3' orientation, with the 5' or 3' terminal nucleotides indicated by a bulbed line above. Sequence logos were created using the weblogo3 server and colors were modified using Adobe illustrator. (E) Hypothetical models of how 3' nucleotide identity influences miRNA strand selection. (Top) The MID domain of Argonaute may directly interact with the 5' nucleotide of the guide strand and the 3' nucleotide of the passenger strand. Such interaction may induce a conformational change that promotes duplex wedging and release of the passenger strand. (Bottom) Alternatively, additional factors may interact with miRNA 3' nucleotides to form a strand selection complex. Dissolution of such complex could facilitate guide strand retention within Argonaute and passenger strand removal.

## Discussion

How does 3' nucleotide identity promote miRNA strand choice? One possibility is that Argonaute directly engages both the 5' nucleotide of the guide strand (*13*, *14*, *25*) and the 3' nucleotide of the passenger strand to initiate duplex unwinding (Fig. 6E). Consistent with this idea, we found that mutating a putative 3' nucleotide binding pocket on Argonaute (*17*) led to an accumulation of some miRNA passenger strands (Fig. S10C). Duplex binding may induce a conformational change of Argonaute, promoting passive wedging by its N-terminal domain (*41*) and coupling nucleotide recognition to duplex unwinding. Notably, mutations in *C. elegans* ALG-1 and its human homolog Ago2 affect miRNA strand asymmetry (*42*, *43*), although it is currently unclear whether those mutations are connected to recognition of 3' nucleotide identity.

An alternative, but not mutually exclusive, hypothesis is that Argonaute cooperates with additional factors that recognize 3' nucleotide identity and bias strand selection (Fig. 6E). For example, the Dicer-interacting proteins TRBP and PACT regulate miRNA strand selection in humans (*44–46*), and Dicer itself can reposition the miRNA duplex after dicing (*45*), raising the possibility that Dicer hands off miRNA duplexes to Argonaute in a favorable orientation. Interestingly, the *C. elegans* genome lacks obvious homologs for both TRPB and PACT, which may at least partially account for the differences in strand selection and 3' nucleotide preferences we observed between *C. elegans* and human cells. More broadly, variation in the protein composition of strand selection complexes could influence miRNA sorting by directing duplexes to distinct Argonaute proteins with different 3’ nucleotide preferences. Although 3' nucleotide identity appears to play a conserved role in miRNA strand selection, it is worth noting that human miRNAs, unlike *C. elegans* miRNAs, lack an obvious global 3' nucleotide asymmetry.

355 This observation highlights the value of model systems such as *C. elegans* in understanding the
356 basic mechanisms of miRNA strand selection.
357
358 In addition to identifying a novel determinant of miRNA strand choice, our findings suggest that
359 3′ nucleotide identity may contribute to the dynamic regulation of miRNA strand asymmetry.
360 While both regulation and dysregulation of miRNA strand asymmetry have previously been
361 reported (see review (*18*)), current models of miRNA strand selection lack a dynamic component
362 to explain context-dependent changes in strand preference (*17*). As 3' isomiRs are typically more
363 frequent than 5' isomiRs (*29*, *47*, *48*), changes in 3' end identity reported in developmental (*29*,
364 *49–51*), cellular (*52*, *53*) or disease (*54*) contexts may underly miRNA strand dynamicity. Some
365 3' modifications, such as miRNA tailing and trimming (*36*, *55*), likely occur after strand selection
366 and are therefore unlikely to affect miRNA strand choice. Other 3' modifications, such as
367 adenylation or uridylation, often target pre-miRNA molecules (*48*, *56–58*) and are more likely to
368 influence strand asymmetry. Consistently, uridylation of human miR-324 leads to altered strand
369 selection, although uridylation of miR-324 may primarily influence Dicer-dependent processing
370 (*59*). Intriguingly, cytidylation of miRNA precursors has been observed in Arabidopsis (*60*) and
371 the miR-83-3p guide strand is cytidylated in *C. elegans* (*55*). As our data indicate that a 3'
372 cytosine on miRNA passenger strands is favorable for strand selection, cytidylation of one strand
373 could bias loading toward the other duplex strand. As these passenger strand modifications
374 would further favor guide strand selection, they are likely to be underrepresented in small RNA
375 sequencing datasets, potentially explaining why such modifications have not yet been identified.
376 Additional work will be needed to fully understand how 3' nucleotides are recognized and how
377 changes in 3' nucleotide identity may regulate miRNA strand selection across different contexts
378 and disrupt miRNA strand selection in human disease.
379
380 **Materials and Methods**
381
382 ***C. elegans* Strains and Genetic Analysis**
383
384 A complete list of *C. elegans* strains used in this study is provided in Table S18. All strains were
385 derived from the wild-type N2 genetic background. Strains were maintained at 20°C under
386 standard growth conditions (*61*). Nematode growth medium (NGM) plates that were seeded with
387 *Escherichia coli* OP50 were used as a food source. For developmental stage-specific analysis,
388 animals were synchronized using standard alkaline hypochlorite treatment (*62*, *63*) and harvested
389 when most (>90%) of the larval population reached the desired developmental stage. For body
390 length measurements, adult animals were imaged on a Leica DM6 upright microscope. Adobe
391 illustrator was used to quantify body length by measuring the path length of a curved line drawn
392 through the center of the animal from the head to base of the tail. For drug assays, young adult
393 worms were added to plates containing 200 µM levamisole (*31*) or 1mM aldicarb (*32*) and
394 scored for paralysis at indicated time intervals. Paralysis was defined as the inability for worms
395 to move in response to a touch stimulus from a platinum wire.
396
397 **Profiling miRNA Duplex Characteristics**
398
399 Mature *C. elegans* and human miRNA sequences were retrieved from miRbase v 22.1 (*37*).
400 Guide and passenger strand annotations were determined based on which strand had the most

401 reported reads on miRbase. 5' nucleotide information was compiled for 5p and 3p strands.
402 RNAcofold from the ViennaRNA Package 2.0 (*64*) was used for duplex folding and to calculate
403 thermodynamic end stability at 20°C as previously described (*28*). Predictions of miRNA strand
404 selection were calculated using twin-drive model as previously described (*17*).
405
406 **CRISPR/Cas9 Genome Editing**
407
408 *Streptococcus pyogenes* Cas9 (IDT, Alt-R® S.p. Cas9 Nuclease V3), single-stranded repair
409 templates (IDT, custom ultramers), crRNA and tracrRNA were commercially sourced. A full list
410 of oligonucleotides used in this study is provided in Table S19. Microinjection and screening
411 were performed using *dpy-10* co-conversion as previously described (*65*). Cas9 was injected at a
412 final concentration of 2.65 µM and all injection mixes included 200 µM KCl and 7.5 µM HEPES
413 [pH 7.4]. All crRNAs were injected at a final concentration of 50 µM, except *dpy-10* crRNA was
414 injected at a final concentration of 5 µM. Equimolar tracrRNA was included in all injection
415 mixes. Single stranded DNA oligonucleotides were used to facilitate homology-directed repair
416 and were included at final concentrations of 6 µM or 3 µM (*dpy-10*).
417
418 **RNA Extraction and Isolation**
419
420 Immediately after sample collection, samples were centrifuged and flash-frozen in liquid
421 nitrogen and stored at -80°C until ready for use. Pellets were thawed in 250 µL RNase-free water
422 (final volume). 1 mL of Trizol (Invitrogen) was added and the mixture was continuously
423 vortexed for 10 minutes. Afterwards, 212 µL of chloroform was added and vortexed for an
424 additional minute. The aqueous and organic layers were separated by centrifugation at 19000 x g
425 for 10 minutes at 4°C. The aqueous phase was then recovered and re-extracted using equal
426 volume of phenol:chloroform:isoamyl alcohol (25:24:1, VWR). The RNA was precipitated for 2
427 hours at -20°C using an equal volume of isopropanol. 1.8 µL of Glycoblue (Invitrogen) was
428 added as a co-precipitant. The RNA pellets were washed using 80% (v/v) ethanol and allowed to
429 air-dry on ice for 10 minutes. The dried pellets were dissolved in RNase-free water and stored at
430 -80°C. RNA concentration was determined using a Nanodrop spectrophotometer.
431
432 **Small RNA Sequencing and Analysis**
433
434 For preparation of small RNA libraries, total RNA was first size selected using a 15% denaturing
435 gel using UreaGel (National Diagnostics) reagents. Single-stranded 18mer
436 (AGCTGCCAGCAACTCTAA) and 26mer (TAGTATGTAGCTGCCAGCAACTCTAA) were
437 combined at a final concentration of 5 µM and used as a molecular ladder in an empty lane. Gels
438 were soaked in 1XTBE solution containing 1X SYBR Gold stain (Invitrogen) for 10 minutes and
439 subsequently visualized under UV light. Small RNAs migrating between the 16mer and 26mer
440 markers were excised from the gel and soaked in 750 µL of TE buffer supplemented with 0.3 M
441 NaCl overnight while shaking at 550 rpm at 7°C. The solution was transferred to a 0.45 µm
442 column and centrifuged at 4°C for 10 minutes at 2500 x g. Small RNAs were precipitated for 2
443 hours at -20°C using equal volume of isopropanol and 10% sample volume 3M NaOAc. 1.5 µL
444 of Glycoblue (Invitrogen) was used as a co-precipitant. The small RNA pellets were washed
445 once using 80% (v/v) ethanol and allowed to air-dry on ice for 10 minutes. The dried pellets
446 were dissolved in 11 µL of RNase-free water. Size-selected small RNA samples were used to

447 make libraries using the Nextflex Small RNA-Seq Kit v3 (PerkinElmer) or the Nextflex Small
448 RNA-Seq Kit v4 (Revvity) according to manufacturer instructions. Please note that the Nextflex
449 Small RNA-Seq Kit v3 (PerkinElmer) was discontinued during this study. We separated small
450 RNA sequencing data acquired from the v3 (Table S5) and v4 kits (Table S6) and only made
451 direct comparisons for samples that were sequenced using the same kit, as we observed
452 differences in normalized read counts for several miRNAs when using different kits. All small
453 RNA libraries were sequenced at the Kansas State University Integrated Genomics Facility using
454 an Illumina NextSeq 500 instrument at 75 cycles.
455
456 Small RNA sequence data were processed and analyzed as previously described (*29*) The
457 cutadapt tool (*66*) was used to process and trim the sequencing reads. The 3' adapter sequences
458 were first removed using the parameters "-a ATCTCGTATGCCGTCTTCTGCTTGX" and
459 demultiplexed using the parameters "e 1 -a file$:barcodes.fasta", where the "barcodes.fasta"
460 contains a list of barcode sequences in fasta format. The 3' primer sequence was then removed
461 from each read using the parameters "-a
462 TGGAATTCTCGGGTGCCAAGGAACTCCAGTCAC". For the Nextflex Small RNA-Seq Kit
463 v3, each end of the processed sequencing reads contained four-nucleotide randomers that were
464 removed using cutadapt. The final four nucleotides of each sequencing read were trimmed using
465 the parameters "-u -4". The first four nucleotides were trimmed using the parameters "-u 4 -m17
466 -M29", which also removed processed reads that were shorter than 17 or longer than 19
467 nucleotides. Read quality was examined using the fastqc tool (*67*). Reads were aligned to a list of
468 mature *C. elegans* miRNAs using bowtie (*68*). The following command was used for bowtie
469 alignments: "-x miR -a --best --strata --norc -v 3", where "miR" is a bowtie build assembled
470 using a fasta file containing all *C. elegans* mature miRNA sequences obtained from miRbase.
471 The samtools tool (*69*) was used to generate, sort and index bam files to generate read count
472 data. A custom bash script was used to identify and quantify isomiR abundance from fastq files.
473 Normalization (reads per million) was performed by multiplying the number of mapped reads for
474 individual miRNA loci by the total number of mapped miRNA reads divided by one million.
475
476 **qPCR and Absolute Quantification**
477
478 The QuantiNova SYBR Green RT-PCR kit (Qiagen) was used for standard qPCR reactions
479 according to manufacturer instructions. Final reaction volumes were adjusted to 5 µL and 100 ng
480 of total *C. elegans* RNA was used as a template. Absolute quantification of miRNAs using
481 Taqman was performed as previously described (*70*). Standard curves were first made using
482 known quantities (0.6ng/µL, $0.6x10^{-2}$ ng/µL, $0.6x10^{-4}$ ng/µL, $0.6x10^{-6}$ ng/µL, and $0.6x10^{-8}$
483 ng/µL) of commercially purchased (IDT) single-stranded RNA oligonucleotides prepared from a
484 2 µg/µL stock. All reactions were carried out at a final volume of 10 µL using the Taqman™
485 MicroRNA Reverse Transcription Kit (Thermofisher) and Taqman™ Universal Master Mix II,
486 no UNG (Thermofisher) according to manufacturer instructions. Custom or predesigned
487 Taqman™ Small RNA Assays (ThermoFisher) were used at 1X final concentration. 1 ng of total
488 *C. elegans* RNA was used as a template for reverse transcription (10 µL reaction volume) and
489 0.67 µL of the cDNA product was used for experimental Taqman assays. The ABI 7500 Real-
490 Time PCR System (Applied Biosystems) was used to run all qPCR and Taqman reactions. A full
491 list of oligonucleotides and Taqman assays used in this study is provided in Table S19.
492

493 **UltramiR Plasmid Construction**
494
495 A full list of plasmids used in this study is provided in Table S20. Each miRNA variant was
496 cloned into the pLMN-ZsGreen-Neomycin-shRNA vector (transOMIC) and transformed into
497 NEB® Stable Competent *E. coli* (High Efficiency) according to manufacturer instructions. The
498 pJM1 through pJM7 plasmids were created by Gibson assembly of
499 Gblock gene fragments (IDT) (Table S19) and HpaI/MluI (NEB) digested pLMN-ZsGreen-
500 Neomycin-shRNA vector using the Gibson Assembly® Cloning Kit (NEB) according to
501 manufacturer instructions. The pJM10 through pJM23 plasmids were created by performing site-
502 directed mutagenesis of the pJM2 plasmid to mutate the nucleotides corresponding to the 3' end
503 of the 5p or 3p strands using the Q5® Site-Directed Mutagenesis Kit (NEB) according to
504 manufacturer instructions. The primers used for site-directed mutagenesis are listed in Table S19.
505 All clones were verified by Sanger sequencing prior to transfection
506
507 **Human Cell Culture and Transfection**
508
509 Human HEK 293T cells were seeded in 12-well plates containing 1 mL DMEM with 10% FBS
510 and transfected when reaching ~90% confluency. In one tube 1 µg of UltramiR plasmid was
511 added to 100 µL of Opti-MEM™ (Thermofisher) and vortexed. In a second tube, 5 µL of 1
512 mg/mL polyethylenimine (PEI) reagent was added to 100 µL of Opti-MEM™ (Thermofisher),
513 vortexed and incubated at room temperature for 5 min. The contents of the second tube were
514 subsequently pipetted into the first tube, vortexed and incubated at room temperature for 15 min.
515 The mixture was then carefully added to the cell media dropwise. After 6 hours, the cell media
516 was changed with fresh warmed DMEM with 10% FBS. 48 hours post-transfection, cells were
517 imaged for ZsGreen expression (Figure S12), harvested in 1 mL of Trizol (Invitrogen), frozen
518 and stored at -80ºC until use.
519
520 **Statistical Analysis**
521
522 R statistical software was used to calculate all statistics. All *P*-values were calculated using two-
523 tailed *t*-tests assuming equal variance among samples. All statistics are presented as mean ± one
524 standard deviation unless otherwise specified.
525
526 **Data Availability**
527
528 Small RNA sequencing data files have been uploaded to the SRA database (PRJNA1378235)
529 and will be released upon final publication. All strains and plasmids used in this study are
530 available upon request. All other data supporting the findings of this study are available from the
531 corresponding author on reasonable request.
532
533 **Acknowledgements**
534
535 We thank members of the Zinovyeva lab for helpful discussions. We thank Hui Tian, Sarah
536 Coffey and Katherine Adams (Hwang) for technical assistance in generating some worm strains,
537 and Alina Akhunova from the Kansas State Integrated Genomics Facility for technical expertise
538 in generating small RNA sequencing data. We are grateful to Anne Hart for sharing *mir-2* mutant

strains. Some of the strains used in this study were provided by the *Caenorhabditis* Genetics Center (CGC) which is funded by NIH Office of Research Infrastructure Programs (P40 OD010440). This work was supported by grants from the National Institutes of Health (R35GM124828 to A.Z. and R01GM117406 to C.M.H.), the Kansas INBRE program (P20 GM103418) and the Johnson Cancer Center at Kansas State University. J.C.M was supported by a fellowship from the NIH (F32GM148040).

**Author Contributions**

J.C.M and A.Z. conceptualized and designed the experiments. A.Z and C.M.H supervised the research and acquired funding. J.C.M, S.K, H.O, H.C, S.Z, W.S, J.S and M.B carried out the experiments. J.C.M and A.Z. performed data analysis and interpreted results. J.C.M and G.P performed the required bioinformatics. J.C.M wrote the original manuscript draft, and all other authors edited the manuscript.

**Competing Interests**

The authors declare no competing interests.

557 **References**
558


559 1. H. Kim, Y.-Y. Lee, V. N. Kim, The biogenesis and regulation of animal microRNAs. *Nat.*
560 *Rev. Mol. Cell Biol.*, 1–21 (2024).

561 2. R. Shang, S. Lee, G. Senavirathne, E. C. Lai, microRNAs in action: biogenesis, function and
562 regulation. *Nat. Rev. Genet.* **24**, 816–833 (2023).

563 3. A. M. Denli, B. B. J. Tops, R. H. A. Plasterk, R. F. Ketting, G. J. Hannon, Processing of
564 primary microRNAs by the Microprocessor complex. *Nature* **432**, 231–235 (2004).

565 4. R. I. Gregory, K. Yan, G. Amuthan, T. Chendrimada, B. Doratotaj, N. Cooch, R. Shiekhattar,
566 The Microprocessor complex mediates the genesis of microRNAs. *Nature* **432**, 235–240 (2004).

567 5. Y. Lee, K. Jeon, J. Lee, S. Kim, V. N. Kim, MicroRNA maturation: stepwise processing and
568 subcellular localization. *EMBO J.* **21**, 4663–4670 (2002).

569 6. Y. Lee, C. Ahn, J. Han, H. Choi, J. Kim, J. Yim, J. Lee, P. Provost, O. Rådmark, S. Kim, V.
570 N. Kim, The nuclear RNase III Drosha initiates microRNA processing. *Nature* **425**, 415–419
571 (2003).

572 7. A. Grishok, A. E. Pasquinelli, D. Conte, N. Li, S. Parrish, I. Ha, D. L. Baillie, A. Fire, G.
573 Ruvkun, C. C. Mello, Genes and Mechanisms Related to RNA Interference Regulate Expression
574 of the Small Temporal RNAs that Control *C. elegans* Developmental Timing. *Cell* **106**, 23–34
575 (2001).

576 8. G. Hutvágner, J. McLachlan, A. E. Pasquinelli, E. Bálint, T. Tuschl, P. D. Zamore, A Cellular
577 Function for the RNA-Interference Enzyme Dicer in the Maturation of the let-7 Small Temporal
578 RNA. *Science* **293**, 834–838 (2001).

579 9. F. Jiang, X. Ye, X. Liu, L. Fincher, D. McKearin, Q. Liu, Dicer-1 and R3D1-L catalyze
580 microRNA maturation in *Drosophila*. *Genes Dev.* **19**, 1674–1679 (2005).

581 10. R. F. Ketting, S. E. J. Fischer, E. Bernstein, T. Sijen, G. J. Hannon, R. H. A. Plasterk, Dicer
582 functions in RNA interference and in synthesis of small RNA involved in developmental timing
583 in *C. elegans. Genes Dev.* **15**, 2654–2659 (2001).

584 11. S. W. Knight, B. L. Bass, A Role for the RNase III Enzyme DCR-1 in RNA Interference and
585 Germ Line Development in *Caenorhabditis elegans*. *Science* **293**, 2269–2271 (2001).

586 12. K. Saito, A. Ishizuka, H. Siomi, M. C. Siomi, Processing of Pre-microRNAs by the Dicer-1–
587 Loquacious Complex in *Drosophila* Cells. *PLoS Biol.* **3**, e235 (2005).

588 13. E. Elkayam, C.-D. Kuhn, A. Tocilj, A. D. Haase, E. M. Greene, G. J. Hannon, L. Joshua-Tor,
589 The Structure of Human Argonaute-2 in Complex with miR-20a. *Cell* **150**, 100–110 (2012).

590 14. N. T. Schirle, I. J. MacRae, The Crystal Structure of Human Argonaute2. *Science* **336**, 1037–
591 1040 (2012).

592 15. A. Nykänen, B. Haley, P. D. Zamore, ATP Requirements and Small Interfering RNA
593 Structure in the RNA Interference Pathway. *Cell* **107**, 309–321 (2001).

594 16. D. S. Schwarz, G. Hutvágner, T. Du, Z. Xu, N. Aronin, P. D. Zamore, Asymmetry in the
595 Assembly of the RNAi Enzyme Complex. *Cell* **115**, 199–208 (2003).

596 17. H. I. Suzuki, A. Katsura, T. Yasuda, T. Ueno, H. Mano, K. Sugimoto, K. Miyazono, Small-
597 RNA asymmetry is directly driven by mammalian Argonautes. *Nat Struct Mol Biol* **22**, 512–521
598 (2015).

599 18. J. C. Medley, G. Panzade, A. Y. Zinovyeva, microRNA strand selection: Unwinding the
600 rules. *Wiley Interdiscip. Rev.: RNA* **12**, e1627 (2021).

601 19. D. T. Humphreys, C. J. Hynes, H. R. Patel, G. H. Wei, L. Cannon, D. Fatkin, C. M. Suter, J.
602 L. Clancy, T. Preiss, Complexity of Murine Cardiomyocyte miRNA Biogenesis, Sequence
603 Variant Expression and Function. *PLoS ONE* **7**, e30933 (2012).

604 20. K. Okamura, M. D. Phillips, D. M. Tyler, H. Duan, Y. Chou, E. C. Lai, The regulatory
605 activity of microRNA* species has substantial influence on microRNA and 3′ UTR evolution.
606 *Nat. Struct. Mol. Biol.* **15**, 354–363 (2008).

607 21. M. Ghildiyal, J. Xu, H. Seitz, Z. Weng, P. D. Zamore, Sorting of Drosophila small silencing
608 RNAs partitions microRNA* strands into the RNA interference pathway. *RNA* **16**, 43–56 (2010).

609 22. S. Kuchen, W. Resch, A. Yamane, N. Kuo, Z. Li, T. Chakraborty, L. Wei, A. Laurence, T.
610 Yasuda, S. Peng, J. Hu-Li, K. Lu, W. Dubois, Y. Kitamura, N. Charles, H. Sun, S. Muljo, P. L.
611 Schwartzberg, W. E. Paul, J. O'Shea, K. Rajewsky, R. Casellas, Regulation of MicroRNA
612 Expression and Abundance during Lymphopoiesis. *Immunity* **32**, 828–839 (2010).

613 23. S. Ro, C. Park, D. Young, K. M. Sanders, W. Yan, Tissue-dependent paired expression of
614 miRNAs. *Nucleic Acids Res.* **35**, 5944–5953 (2007).

615 24. J.-S. Yang, M. D. Phillips, D. Betel, P. Mu, A. Ventura, A. C. Siepel, K. C. Chen, E. C. Lai,
616 Widespread regulatory activity of vertebrate microRNA* species. *RNA* **17**, 312–326 (2011).

617 25. F. Frank, N. Sonenberg, B. Nagar, Structural basis for 5′-nucleotide base-specific recognition
618 of guide RNA by human AGO2. *Nature* **465**, 818–822 (2010).

619 26. A. Khvorova, A. Reynolds, S. D. Jayasena, Functional siRNAs and miRNAs Exhibit Strand
620 Bias. *Cell* **115**, 209–216 (2003).

621 27. M. B. Warf, W. E. Johnson, B. L. Bass, Improved annotation of *C. elegans* microRNAs by
622 deep sequencing reveals structures associated with processing by Drosha and Dicer. *RNA* **17**,
623 563–577 (2011).

624 28. J. C. Medley, A. Zinovyeva, In silico unwinding of *Caenorhabditis elegans* microRNA
625 duplexes to evaluate thermodynamic end stabilities improves predictions of microRNA strand
626 selection. *bioRxiv*, 2025.06.26.661848 (2025).

627 29. G. Panzade, L. Li, S. Hebbar, I. Veksler-Lublinsky, A. Zinovyeva, Global profiling and
628 annotation of templated isomiRs dynamics across *Caenorhabditis elegans* development. *RNA*
629 *Biol.* **19**, 928–942 (2022).

630 30. E. Alvarez-Saavedra, H. R. Horvitz, Many Families of C. elegans MicroRNAs Are Not
631 Essential for Development or Viability. *Curr Biol* **20**, 367–373 (2010).

632 31. D. J. Simon, J. M. Madison, A. L. Conery, K. L. Thompson-Peer, M. Soskis, G. B. Ruvkun,
633 J. M. Kaplan, J. K. Kim, The MicroRNA miR-1 Regulates a MEF-2-Dependent Retrograde
634 Signal at Neuromuscular Junctions. *Cell* **133**, 903–915 (2008).

635 32. P. J. O'Hern, I. do C. G. Gonçalves, J. Brecht, E. J. L. Soto, J. Simon, N. Chapkis, D.
636 Lipscombe, M. J. Kye, A. C. Hart, Decreased microRNA levels lead to deleterious increases in
637 neuronal M2 muscarinic receptors in Spinal Muscular Atrophy models. *eLife* **6**, e20752 (2017).

638 33. A. Lingel, B. Simon, E. Izaurralde, M. Sattler, Nucleic acid 3′-end recognition by the
639 Argonaute2 PAZ domain. *Nat. Struct. Mol. Biol.* **11**, 576–577 (2004).

640 34. Y. Wang, G. Sheng, S. Juranek, T. Tuschl, D. J. Patel, Structure of the guide-strand-
641 containing argonaute silencing complex. *Nature* **456**, 209–13 (2008).

642 35. S. L. Ameres, P. D. Zamore, Diversifying microRNA sequence and function. *Nat. Rev. Mol.*
643 *Cell Biol.* **14**, 475–488 (2013).

644 36. J. Han, J. T. Mendell, MicroRNA turnover: a tale of tailing, trimming, and targets. *Trends*
645 *Biochem. Sci.* **48**, 26–39 (2023).

646 37. A. Kozomara, M. Birgaoanu, S. Griffiths-Jones, miRBase: from microRNA sequences to
647 function. *Nucleic Acids Res.* **47**, D155–D162 (2018).

648 38. A. Creugny, A. Fender, S. Pfeffer, Regulation of primary microRNA processing. *FEBS Lett.*
649 **592**, 1980–1996 (2018).

650 39. J. Han, Y. Lee, K.-H. Yeom, Y.-K. Kim, H. Jin, V. N. Kim, The Drosha-DGCR8 complex in
651 primary microRNA processing. *Genes Dev.* **18**, 3016–3027 (2004).

652 40. S. R. V. Knott, A. R. Maceli, N. Erard, K. Chang, K. Marran, X. Zhou, A. Gordon, O.
653 El Demerdash, E. Wagenblast, S. Kim, C. Fellmann, G. J. Hannon, A Computational Algorithm
654 to Predict shRNA Potency. *Mol. Cell* **56**, 796–807 (2014).

655 41. P. B. Kwak, Y. Tomari, The N domain of Argonaute drives duplex unwinding during RISC
656 assembly. *Nat Struct Mol Biol* **19**, 145–151 (2012).

657 42. Y. Duan, L. Li, G. P. Panzade, A. Piton, A. Zinovyeva, V. Ambros, Modeling
658 neurodevelopmental disorder-associated human AGO1 mutations in *Caenorhabditis elegans*
659 Argonaute *alg-1*. *Proc. Natl. Acad. Sci.* **121**, e2308255121 (2024).

660 43. A. Y. Zinovyeva, I. Veksler-Lublinsky, A. A. Vashisht, J. A. Wohlschlegel, V. R. Ambros,
661 *Caenorhabditis elegans* ALG-1 antimorphic mutations uncover functions for Argonaute in
662 microRNA guide strand selection and passenger strand disposal. *Proc. Natl. Acad. Sci.* **112**,
663 E5271–E5280 (2015).

664 44. Y. Kim, J. Yeo, J. H. Lee, J. Cho, D. Seo, J.-S. Kim, V. N. Kim, Deletion of human tarbp2
665 reveals cellular microRNA targets and cell-cycle function of TRBP. *Cell Reports* **9**, 1061–74
666 (2014).

667 45. C. L. Noland, J. A. Doudna, Multiple sensors ensure guide strand selection in human RNAi
668 pathways. *RNA* **19**, 639–648 (2013).

669 46. R. C. Wilson, A. Tambe, M. A. Kidwell, C. L. Noland, C. P. Schneider, J. A. Doudna, Dicer-
670 TRBP Complex Formation Ensures Accurate Mammalian MicroRNA Biogenesis. *Mol. Cell* **57**,
671 397–407 (2015).

672 47. M. A. Newman, V. Mani, S. M. Hammond, Deep sequencing of microRNA precursors
673 reveals extensive 3′ end modification. *RNA* **17**, 1795–1803 (2011).

674 48. S. K. Wyman, E. C. Knouf, R. K. Parkin, B. R. Fritz, D. W. Lin, L. M. Dennis, M. A.
675 Krouse, P. J. Webster, M. Tewari, Post-transcriptional generation of miRNA variants by multiple
676 nucleotidyl transferases contributes to miRNA transcriptome complexity. *Genome Res* **21**, 1450–
677 61 (2011).

678 49. D. Fernández-Pérez, M. A. Brieño-Enríquez, J. Isoler-Alcaraz, E. Larriba, J. del Mazo,
679 MicroRNA dynamics at the onset of primordial germ and somatic cell sex differentiation during
680 mouse embryonic gonad development. *Rna* **24**, 287–303 (2018).

681 50. S. L. Fernandez-Valverde, R. J. Taft, J. S. Mattick, Dynamic isomiR regulation in
682 *Drosophila* development. *RNA* **16**, 1881–1888 (2010).

683 51. A. C. de Oliveira, L. A. Bovolenta, L. Figueiredo, A. D. O. Ribeiro, B. J. A. Pereira, T. R. A.
684 de Almeida, V. F. Campos, J. G. Patton, D. Pinhal, MicroRNA Transcriptomes Reveal
685 Prevalence of Rare and Species-Specific Arm Switching Events During Zebrafish Ontogenesis.
686 *Evol. Bioinform. Online* **20**, 11769343241263230 (2024).

687 52. E. Londin, P. Loher, A. G. Telonis, K. Quann, P. Clark, Y. Jing, E. Hatzimichael, Y. Kirino,
688 S. Honda, M. Lally, B. Ramratnam, C. E. S. Comstock, K. E. Knudsen, L. Gomella, G. L.
689 Spaeth, L. Hark, L. J. Katz, A. Witkiewicz, A. Rostami, S. A. Jimenez, M. A. Hollingsworth, J.
690 J. Yeh, C. A. Shaw, S. E. McKenzie, P. Bray, P. T. Nelson, S. Zupo, K. V. Roosbroeck, M. J.
691 Keating, G. A. Calin, C. Yeo, M. Jimbo, J. Cozzitorto, J. R. Brody, K. Delgrosso, J. S. Mattick,
692 P. Fortina, I. Rigoutsos, Analysis of 13 cell types reveals evidence for the expression of
693 numerous novel primate- and tissue-specific microRNAs. *Proc. Natl. Acad. Sci.* **112**, E1106–
694 E1115 (2015).

695 53. C. M. Smith, G. Hutvagner, A comparative analysis of single cell small RNA sequencing
696 data reveals heterogeneous isomiR expression and regulation. *Sci. Rep.* **12**, 2834 (2022).

697 54. A. G. Telonis, R. Magee, P. Loher, I. Chervoneva, E. Londin, I. Rigoutsos, Knowledge about
698 the presence or absence of miRNA isoforms (isomiRs) can successfully discriminate amongst 32
699 TCGA cancer types. *Nucleic Acids Res.* **45**, 2973–2985 (2017).

700 55. K.-F. Vieux, K. P. Prothro, L. H. Kelley, C. Palmer, E. M. Maine, I. Veksler-Lublinsky, K.
701 McJunkin, Screening by deep sequencing reveals mediators of microRNA tailing in *C. elegans*.
702 *Nucleic Acids Res* **49**, gkab840- (2021).

703 56. A. M. Burroughs, Y. Ando, M. J. L. de Hoon, Y. Tomaru, T. Nishibu, R. Ukekawa, T.
704 Funakoshi, T. Kurokawa, H. Suzuki, Y. Hayashizaki, C. O. Daub, A comprehensive survey of 3′
705 animal miRNA modification events and a possible role for 3′ adenylation in modulating miRNA
706 targeting effectiveness. *Genome Res.* **20**, 1398–1410 (2010).

707 57. I. Heo, C. Joo, J. Cho, M. Ha, J. Han, V. N. Kim, Lin28 Mediates the Terminal Uridylation
708 of let-7 Precursor MicroRNA. *Mol. Cell* **32**, 276–284 (2008).

709 58. I. Heo, M. Ha, J. Lim, M.-J. Yoon, J.-E. Park, S. C. Kwon, H. Chang, V. N. Kim, Mono-
710 Uridylation of Pre-MicroRNA as a Key Step in the Biogenesis of Group II let-7 MicroRNAs.
711 *Cell* **151**, 521–532 (2012).

712 59. H. Kim, J. Kim, S. Yu, Y.-Y. Lee, J. Park, R. J. Choi, S.-J. Yoon, S.-G. Kang, V. N. Kim, A
713 Mechanism for microRNA Arm Switching Regulated by Uridylation. *Mol Cell* **78**, 1224-1236.e5
714 (2020).

715 60. J. Song, X. Wang, B. Song, L. Gao, X. Mo, L. Yue, H. Yang, J. Lu, G. Ren, B. Mo, X. Chen,
716 Prevalent cytidylation and uridylation of precursor miRNAs in *Arabidopsis*. *Nat. Plants* **5**, 1260–
717 1272 (2019).

718 61. S. Brenner, The Genetics of *Caenorhabditis elegans*. *Genetics* **77**, 71–94 (1974).

719 62. J. D. Hibshman, A. K. Webster, L. R. Baugh, Liquid-culture protocols for synchronous
720 starvation, growth, dauer formation, and dietary restriction of *Caenorhabditis elegans*. *STAR*
721 *Protoc.* **2**, 100276 (2021).

722 63. M. Porta-de-la-Riva, L. Fontrodona, A. Villanueva, J. Cerón, Basic *Caenorhabditis elegans*
723 methods: synchronization and observation. *J. Vis. Exp. : JoVE*, e4019 (2012).

724 64. R. Lorenz, S. H. Bernhart, C. H. Z. Siederdissen, H. Tafer, C. Flamm, P. F. Stadler, I. L.
725 Hofacker, ViennaRNA Package 2.0. *Algorithms Mol. Biol. : AMB* **6**, 26 (2011).

726 65. A. Paix, A. Folkmann, D. Rasoloson, G. Seydoux, High Efficiency, Homology-Directed
727 Genome Editing in *Caenorhabditis elegans* Using CRISPR-Cas9 Ribonucleoprotein Complexes.
728 *Genetics* **201**, 47–54 (2015).

729 66. M. Martin, Cutadapt removes adapter sequences from high-throughput sequencing reads.
730 *EMBnetJ.* **17**, 10–12 (2011).

731 67. Andrews, FastQC: A Quality Control Tool for High Throughput Sequence Data. *Available*
732 *online at: http://www.bioinformatics.babraham.ac.uk/projects/fastqc/* (2010).

733 68. B. Langmead, C. Trapnell, M. Pop, S. L. Salzberg, Ultrafast and memory-efficient alignment
734 of short DNA sequences to the human genome. *Genome Biol.* **10**, R25–R25 (2009).

735 69. H. Li, B. Handsaker, A. Wysoker, T. Fennell, J. Ruan, N. Homer, G. Marth, G. Abecasis, R.
736 Durbin, 1000 Genome Project Data Processing Subgroup, The Sequence Alignment/Map format
737 and SAMtools. *Bioinformatics* **25**, 2078–2079 (2009).

738 70. B. F. Donnelly, B. Yang, A. L. Grimme, K.-F. Vieux, C.-Y. Liu, L. Zhou, K. McJunkin, The
739 developmentally timed decay of an essential microRNA family is seed-sequence dependent. *Cell*
740 *Rep.* **40**, 111154–111154 (2022).

741